Data-Driven Motion Compensation for Airborne Bistatic SAR Imagery Under Fast Factorized Back Projection Framework

Min Bao, *Member, IEEE*, Song Zhou, *Member, IEEE*, Lei Yang, *Member, IEEE*, Mengdao Xing, *Fellow, IEEE*, and Lifan Zhao

***Abstract*—Due to the independence of azimuth invariance and high implementing efficiency, a fast time-domain algorithm has significant advantages for airborne bistatic synthetic aperture radar (BiSAR) data process with general geometric configuration. In this article, the practical problem of unexpected motion errors of the airborne platform is carefully analyzed under a fast factorized back-projection (FFBP) framework for a general BiSAR process and a coherent data-driven motion compensation (MOCO) algorithm integrated with FFBP is proposed. By utilizing wavenumber decomposition, the analytical spectrum of a polar grid image is obtained where the motion error can be conveniently investigated in image spectrum domain and the coherence between azimuthal phase error (APE) and motion-induced nonsystematic range cell migration (NsRCM) can be perfectly revealed. Then, a new data-driven MOCO method for both APE and NsRCM correction is developed with the FFBP process. Different from the data-driven MOCO in most frequency-domain algorithms, the residual NsRCM introduced by the FFBP process is particularly analyzed and addressed in the MOCO, which significantly improves the image quality in focusing. Promising results from both simulation and raw data experiments are presented and analyzed to validate the advantages of the proposed algorithm for the airborne BiSAR process.**

***Index Terms*—Bistatic synthetic aperture radar (BiSAR), fast factorized back projection (FFBP), motion compensation (MOCO), nonsystematic range cell migration (NsRCM).**

Manuscript received January 8, 2020; revised May 5, 2020; accepted June 10, 2020. Date of publication June 15, 2020; date of current version January 18, 2021. This work was supported in part by the National Natural Science Foundation of China under Grant 61201284, in part by Shaanxi Innovative Talents Promotion Plan-Science and Technology Innovation Team under Grant 2019TD-002, in part by the Fundamental Research Funds for the Central Universities under Grant JB190204, in part by the National Natural Science Foundation of China under Grant 61801204 and Grant 61601470, in part by the Natural Science Foundation of Tianjin, China, under Grant 20162898 (16JCYBJC41200), and in part by the public foundation from Key Laboratory of EMW Information, Fudan University, China, under Grant EMW201901. *(Corresponding author: Min Bao.)*

Min Bao is with the School of Electronic Engineering, Xidian University, Xi'an 710071, China (e-mail: mbao@xidian.edu.cn).

Song Zhou is with the School of Information Engineering, Nanchang University, Nanchang 330031, China (e-mail: zhousong8411@sina.com).

Lei Yang is with the Tianjin Key Lab for Advanced Signal Processing, Civil Aviation University of China, Tianjin 300300, China (e-mail: yanglei840626@163.com).

Mengdao Xing is with the National Laboratory of Radar Signal Processing and the Collaborative Innovation Center of Information Sensing and Understanding, Xidian University, Xi'an 710071, China (e-mail: xmd@xidian.edu.cn).

Lifan Zhao is with the School of Electrical and Electronic Engineering, Nanyang Technological University 639798, Singapore (e-mail: zhao01145@e.ntu.edu.sg).

Digital Object Identifier 10.1109/JSTARS.2020.3002394

I. Introduction

DUE to the observing ability in all weather and all day-and-night, synthetic aperture radar (SAR) has become a significant tool for microwave remote sensing [1]. Bistatic SAR (BiSAR) is a kind of SAR system in which the transmitter and the receiver are separated on different platforms [2]. Comparing with the conventional monostatic SAR, BiSAR has many advantages, such as flexible geometric configuration, obtaining more scattering information, as well as reduced vulnerability in military applications. Moreover, by placing transmitter and receiver with a proper geometric configuration, BiSAR can work in forward-looking mode [3], [4], which has significant application potential in terminal guidance and attacking, aircraft navigation, and self-landing [5]. Thus, BiSAR technique attracts growing interest in recent years.

Comparing with traditional monostatic SAR, an algorithm for BiSAR imaging is more complicated due to the flexible bistatic configuration and complex signal property [6], [7]. Similar as monostatic SAR, the imaging algorithms for BiSAR can be also divided into frequency-domain algorithm (FDA) and time-domain algorithm (TDA) categories. FDA includes range-Doppler algorithm, chirp-scaling algorithm, Omega-K algorithm, etc., which originates from monostatic SAR processing, and these algorithms have been extended to many BiSAR applications with high computational efficiency. However, most FDAs are based on the classic azimuth-invariant assumptions that may not valid in BiSAR applications, such as the cases of an SAR system operating in a nonlinear trajectory with varying platform velocities [8], general geometric configurations, etc., which introduces difficulties to the FDA process. Although motion compensation (MOCO) techniques can be applied with an FDA to improve the focusing quality to some extent [9], [10], they are usually insufficient to achieve promising results in high-resolution and high-precision applications [11]. This is due to the fact that most FDAs are based on the foundation of azimuth-invariant assumption, e.g., bistatic platforms move along linear trajectory with the same and constant velocity. However, in the case of platforms moving along a nonlinear trajectory with different velocities, it can be regarded that the signal model of FDA contains huge motion errors from the case of linear trajectory with the same and constant velocity. In the FDA process, these huge motion errors as well as their adverse

effects need to be exactly compensated, which will bring a lot of difficulties in MOCO development. In contrast, the signal model of a TDA can be based on a nonlinear trajectory with different velocities, thus the motion error in the signal model of the TDA can be regarded as a small component, which will facilitate the MOCO development. This motivates us to research on a TDA for obtaining better imaging performance.

A TDA is the other significant trend for BiSAR with general configurations [12]. Because the geometry as well as trajectory designation of BiSAR is much more flexible than monostatic SAR, a TDA has significant performance advantages due to its independence of azimuth-invariant assumption and avoidance of complex range-azimuth coupling problems [11], [13]. Back projection (BP) is a well-known TDA, which has high-accuracy imaging performance and has been well applied in practical systems. However, the main drawback of huge computational burden makes it inconvenient to develop real-time processor. Methods for improvements have been suggested to provide fast implementations [14]. A fast factorized BP (FFBP) algorithm and its modifications are a kind of the most popular fast TDA, which can dramatically reduce the computation burden and maintain the accuracy and applicability of a BP algorithm [15]. Moreover, due to the inherent processing architecture, FFBP can be further accelerated by implementing the algorithm on parallel processors for real-time operation [11]. These advantages motivate us to study an FFBP algorithm for BiSAR applications.

To apply FFBP to airborne BiSAR application, the motion error problem needs to be considered [16], especially for the low-cost and small-size platform without a high-accuracy navigation system, such as the global positioning system (GPS) and inertial navigation system [17], [18]. Generally, the influence of platform vibration, wind field as well as turbulence will introduce unknown motion errors [19]. Thus, it is preferable to integrate data-driven MOCO into the FFBP process to address a motion error problem. In [20], a factorized geometrical autofocus algorithm with an FFBP formation was proposed for ultrawide bandwidth SAR applications, which can obtain well-focused results from CARABAS II data set by exhaustive search routine. In [21], an autofocusing method based coordinate descent and secant processing was proposed and integrated with FFBP, which can effectively improve the focusing performance for monostatic SAR application. However, it cannot be directly utilized in BiSAR with general configuration. In [22], an optimization-based MOCO is proposed and incorporated with the FFBP process for bistatic forward-looking SAR with high accuracy. However, in the case of intense motion error, the searching procedures may increase the computational burden obviously. In [23], a multiple-aperture-based map-drift MOCO algorithm was proposed to integrate with the FFBP process, which can efficiently compensate for the motion error to improve the quality in focusing. However, it is difficult to correct the nonsystematic range cell migration (NsRCM) [24], [25] in the algorithm so that it cannot be applied to the high-resolution BiSAR with severe motion errors. Zhou *et al.* [26] introduced a quasi-polar-based FFBP for miniature unmanned aerial vehicle (UAV)-SAR where the NsRCM can be exactly correctly by deriving the relationship between azimuthal phase error (APE) and NsRCM. However, the algorithm cannot be directly utilized in the BiSAR process. Therefore, it remains to be a challenge to effectively and efficiently incorporate data-driven MOCO into FFBP for the BiSAR process with a general configuration.

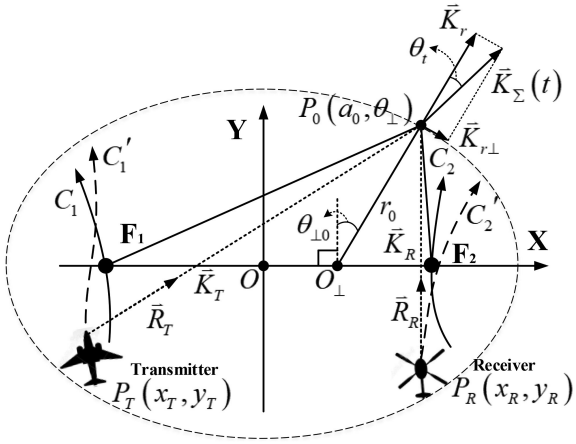

Fig. 1. Geometry in the OEP coordinate system.

In this article, a new data-driven MOCO algorithm is proposed and integrated with the FFBP process for general BiSAR imaging. In previous research for the BiSAR process, it was demonstrated that the FFBP recursing in orthogonal elliptical polar (OEP) grid has reduced computational burden than that in traditional elliptical polar grid [27]. Thus, in this article, both MOCO and FFBP are developed in an OEP coordinate system. By utilizing wavenumber decomposition, the analytical spectrum of image in OEP is derived based on which the influence of motion error to the FFBP process can be conveniently investigated and the coherence between APE and NsRCM under an FFBP framework can be perfectly revealed. Based on the coherence, a coherent data-driven MOCO for both APE and NsRCM compensation is developed with the FFBP process. Different from the data-driven MOCO in most FDAs, the residual NsRCM introduced in the FFBP process is particularly analyzed and addressed, which significantly improves the image quality in focusing for high-resolution BiSAR application. Both simulation data and raw data set acquired from a BiSAR test bed are utilized to evaluate the proposed algorithm, and the experimental results show its performance superiority in practical applications.

The rest of this article is organized as follows. The BiSAR geometry and signal model are introduced in Section II. In Section III, the analytical spectrum of image is derived and the influence of motion error in spectrum domain is accordingly investigated. The coherence between APE and NsRCM is revealed and analyzed in Section IV and the processing diagram of the MOCO algorithm is described in Section V. Simulation experiment and raw data experiments are provided and analyzed in Section VI. Finally, the conclusion is drawn in Section VII.

II. Geometry and Signal Model

Fig. 1 shows the airborne BiSAR with a general geometry. Here, we assume a 2-D geometry model to simplify the derivation and signal analyses. In practical applications, the tomography information needs to be utilized and integrated in

the process [11]. Assuming that, the transmitter and receiver are mounted on two airborne platforms, respectively. First, we consider the ideal case in which both platforms moving along the expected trajectories without motion error, denoted by the solid curves, C_1 and C_2, respectively. Let t denote the azimuth time. At t, the antenna phase center (APC) of the transmitter is at $P_T(x_T, y_T)$, whereas the APC of the receiver is at $P_R(x_R, y_R)$, where x_T, y_T, x_R, and y_R can be regarded as functions with variable of t, and it has

$$\begin{cases} x_T = x_T(t) \\ x_R = x_R(t) \\ y_T = y_T(t) \\ y_R = y_R(t). \end{cases} \tag{1}$$

At t, the echoes from an arbitrary scatterer $P_0(x_0, y_0)$ with a constant reflectivity coefficient α in the illuminating scenario can be given as

$$S(t, K) = \alpha \exp[-j(R_{T0} + R_{R0})K] \tag{2}$$

where K is the magnitude of wavenumber related to the transmitted signal, and it has

$$K = \frac{2\pi}{c}(f_c + f_r) \tag{3}$$

where c is the speed of light, f_c is the carrier frequency, and f_r is the fast-time frequency. In (2), R_{T0} is the range from P_T to P_0, and R_{R0} is the range from P_R to P_0, and it has

$$R_{T0} = \sqrt{(x_0 - x_T)^2 + (y_0 - y_T)^2} \tag{4}$$

and

$$R_{R0} = \sqrt{(x_0 - x_R)^2 + (y_0 - y_R)^2}. \tag{5}$$

To facilitate the signal analyses in an FFBP framework, wavenumber vectors as well as range vectors are introduced to reformulate the echoed signal. Then, (2) can be rewritten as

$$S(t, K_r) = \alpha \exp\left(-j\vec{R}_{T0} \cdot \vec{K}_T - j\vec{R}_{R0} \cdot \vec{K}_R\right) \tag{6}$$

where "$\cdot$" denotes inner product operation. In (6), $\vec{K}_T$ is the wavenumber vector with the direction from P_T to P_0, while $\vec{K}_R$ is the wavenumber vector with the direction from P_R to P_0. $\vec{K}_T$ and $\vec{K}_R$ have the same magnitude of K, but their directions vary with azimuth time t. $\vec{R}_{T0}$ is the range vector from P_T to P_0, and $\vec{R}_{R0}$ is the range vector from P_R to P_0. The magnitudes of $\vec{R}_{T0}$ and $\vec{R}_{R0}$ are given by (4) and (5), respectively.

Assuming that in the BP operation, the echoes are projected onto Cartesian grids (x, y) to form an SAR image and the BP image can be given by the following integral [28]:

$$i(x, y) = \int s(t, R_\Sigma)|_{R_\Sigma = R_T + R_R} dt \tag{7}$$

where

$$s(t, R_\Sigma) = \int S(t, K) \exp(jR_\Sigma K)\, dK. \tag{8}$$

Different from (4) and (5), R_T in (7) and (8) is the range from P_T to the image grid $P(x, y)$ and R_R is the range from P_R to the image grid $P(x, y)$. For R_T and R_R, it has

$$R_T = \sqrt{(x - x_T)^2 + (y - y_T)^2} \tag{9}$$

and

$$R_R = \sqrt{(x - x_R)^2 + (y - y_R)^2}. \tag{10}$$

In (7) and (8), R_Σ can be given as

$$R_\Sigma = R_T + R_R. \tag{11}$$

With (2) and (8)–(11), (7) can be rewritten as

$$\begin{aligned} i(x, y) = \int\int \alpha \exp\Big[& -j\sqrt{(x_0 - x_T)^2 + (y_0 - y_T)^2}K \\ & - j\sqrt{(x_0 - x_R)^2 + (y_0 - y_R)^2}K\Big] \\ & \times \exp\Big[j\sqrt{(x - x_T)^2 + (y - y_T)^2}K \\ & + j\sqrt{(x - x_R)^2 + (y - y_R)^2}K\Big] dK dt. \end{aligned} \tag{12}$$

Let $\vec{R}_T$ denote the range vector from P_T to P, and $\vec{R}_R$ the range vector from P_R to P. The magnitudes of $\vec{R}_T$ and $\vec{R}_R$ are given by (9) and (10), respectively. Then, (12) can be reformed as

$$\begin{aligned} i(x, y) = \int\int \alpha \exp & \left(-j\vec{R}_{T0} \cdot \vec{K}_T - j\vec{R}_{R0} \cdot \vec{K}_R\right) \\ & \times \exp\left(j\vec{R}_T \cdot \vec{K}_T + j\vec{R}_R \cdot \vec{K}_R\right) dK dt. \end{aligned} \tag{13}$$

Expression (13) is the refined BP integral in wavenumber representation. Then, we consider the real case with a motion error, as shown in Fig. 1. In Fig. 1, the real trajectories of the transmitter and receivers are denoted by the dashed curves C_1' and C_2', respectively. Let $\Delta\vec{R}_T$ denotes the motion error of the transmitter, whereas $\Delta\vec{R}_R$ denotes the motion error of the receiver. $\Delta\vec{R}_T$ and $\Delta\vec{R}_R$ represent the deviations of the real trajectories from the expected trajectories. Both $\Delta\vec{R}_T$ and $\Delta\vec{R}_R$ can be regarded as functions of azimuth time t as

$$\begin{cases} \Delta\vec{R}_T = \Delta\vec{R}_T(t) \\ \Delta\vec{R}_R = \Delta\vec{R}_R(t). \end{cases} \tag{14}$$

Generally, it has $|\Delta\vec{R}_T| << |\vec{R}_{T0}|$ and $|\Delta\vec{R}_R| << |\vec{R}_{R0}|$, so that the wavenumber vector from P_T' to P_0 can be approximated by $\vec{K}_T$, and the wavenumber vector from P_T' to P_0 can be also approximated by $\vec{K}_R$. Originated from the ideal model of (13), the BP integral can be approximated by

$$\begin{aligned} i(x, y) \approx \int\int \alpha \exp & \Big[-j\left(\Delta\vec{R}_T + \Delta\vec{R}_{T0}\right) \cdot \vec{K}_T \\ & - j\left(\Delta\vec{R}_R + \vec{R}_{R0}\right) \cdot \vec{K}_R\Big] \\ & \times \exp\left(j\vec{R}_T \cdot \vec{K}_T + j\vec{R}_R \cdot \vec{K}_R\right) dK dt. \end{aligned} \tag{15}$$

Equation (15) can be also manipulated as

$$i(x,y) \approx \int\int \alpha \exp\left(-j\Delta\vec{R}_T \cdot \vec{K}_T - j\Delta\vec{R}_R \cdot \vec{K}_R\right) \times \exp\left[-j\left(\vec{R}_{T0} - \vec{R}_T\right) \cdot \vec{K}_T\right] \times \exp\left[-j\left(\vec{R}_{R0} - \vec{R}_R\right) \cdot \vec{K}_R\right] dKdt. \quad (16)$$

Let $\vec{R}_0$ denote the range vector from the origin O to P_0 and $\vec{R}$ the range vector from O to P. So that $(\vec{R}_0 - \vec{R})$ denotes the range vector from P to P_0, and it has

$$\vec{R}_0 - \vec{R} = \vec{R}_{T0} - \vec{R}_T = \vec{R}_R - \vec{R}_R. \quad (17)$$

Then, let $\vec{K}_\Sigma$ be the combined wavenumber vector from $\vec{K}_T$ and $\vec{K}_R$ as

$$\vec{K}_\Sigma = \vec{K}_T + \vec{K}_R. \quad (18)$$

With (17) and (18), (16) can be rewritten as

$$i(x,y) \approx \int\int \alpha \exp\left(-j\Delta\vec{R}_T \cdot \vec{K}_T - j\Delta\vec{R}_R \cdot \vec{K}_R\right) \times \exp\left[-j\left(\vec{R}_0 - \vec{R}\right) \cdot \vec{K}_\Sigma\right] dKdt. \quad (19)$$

In (19), the first exponential term is introduced by the motion error that will adversely affect the focusing quality in final image, whereas the second exponential term is the intrinsic term from the BP integral. In the second exponential term, $(\vec{R}_0 - \vec{R})$ also indicates the location of P_0 focused on the image plane after the BP process. In the following sections, the influence of motion errors to the FFBP process will be investigated carefully and an effective and efficiency data-driven MOCO will be developed.

III. Image Spectrum Analyses With Motion Error in the OEP Grid

Different from the direct BP algorithm operating in the Cartesian coordinate system, the FFBP algorithm operates in the Polar coordinate system where the image spectrum from subaperture can be compacted into a narrower range so that the Nyquist sampling requirement can be significantly decreased and the computational burden can be consequently reduced [13]. In our previous research for the BiSAR process, we proposed an OEP system where the FFBP algorithm has reduced time consumption compared with the conventional FFBP algorithm [27]. In this section, we will investigate the influence of motion errors to the FFBP process operating in the OEP coordinates system.

Here, we first give a brief view of the OEP coordinate system in FFBP for the BiSAR process. Assume that P_0 is the center of the illuminated scenario and the OEP system is established based on P_0, as shown in Fig. 1. In the OEP system, the origin is defined at $O_\perp$, and $\angle F_1P_0F_2$ is equally divided by $\vec{O_\perp P_0}$. $\theta_{\perp 0}$ is the angle between $\vec{O_\perp P_0}$ and the major axis, and the coordinates of P_0 is represented as $(a_0, \theta_{\perp 0})$, where a_0 is defined by

$$a_0 = \frac{1}{2}\left(\left|\vec{F_1P_0}\right| + \left|\vec{F_2P_0}\right|\right). \quad (20)$$

where F_1 and F_2 are the focus of the ellipse, and $|\cdot|$ denotes the magnitude calculation for the vector. For an arbitrary grid in the OEP system, the coordinates in OEP is represented as $(a, \theta_\perp)$ and the SAR image represented in OEP is given by $i(a, \theta_\perp)$, where a is the major axis coordinate and $\theta_\perp$ is the angular coordinate. So far, the OEP system is established. Because the wavenumber vector of a signal can be decomposed in an orthogonal system, the image spectrum in both range and angular directions has a narrowest range. Details of advantages of the OEP system can be found in [27].

Because the FFBP for BiSAR recurses on the OEP system, the data-driven MOCO is also developed based on the OEP system. In current data-driven MOCO methods, e.g., phase gradient autofocusing (PGA) [29] and map-drift autofocusing [17], the phase errors are generally estimated and compensated in their spectrum domains, i.e., range-compressed azimuth-frequency domain. However, in BP and FFBP process, the echoed signal is projected on the designed image grid and the SAR image is directly obtained. Thus it is necessary to investigate the image spectrum as well as the influence of motion error in image spectrum domain for autofocusing implementation. It is also emphasized that we develop data-driven MOCO in $I(a, K_\theta)$ domain rather than $I(K_x, y)$ domain with respect to $i(x, y)$. This is due to the fact that, in $I(a, K_\theta)$ domain, the echoes' energy is nearly all around $K_\theta = 0$, which makes the phase autofocusing easy to process. However, in $I(K_x, y)$ domain, the echoes' energy is spread into different K_x range that bring difficulty to the phase autofocusing process. Therefore, we first derive the analytical spectrum of image in $I(a, K_\theta)$ domain, then develop data-driven MOCO in $I(a, K_\theta)$ domain.

To derive the image spectrum, we introduce a pair of wavenumber vectors, denoted as $\vec{K}_r$ and $\vec{K}_{r\perp}$, respectively. $\vec{K}_r$ is along $\vec{O_\perp P_0}$ direction, whereas $\vec{K}_{r\perp}$ is along the tangent of the ellipse across P_0. $\vec{K}_r$ and $\vec{K}_{r\perp}$ are perpendicular with each other. Then, the combined wavenumber vector in (19) can be decomposed as

$$\vec{K}_\Sigma = \vec{K}_r + \vec{K}_{r\perp}. \quad (21)$$

The other wavenumber vectors as well as range vectors can be also decomposed along as $\vec{K}_r$ and $\vec{K}_{r\perp}$ directions. Then, the following integral can be obtained from (19) as:

$$i(a, \theta_\perp) \approx \int\int \alpha \exp\left(-j\Delta R_{r\perp}K_{r\perp} - j\Delta R_r \cos\beta_0 K_a\right) \times \exp\left(-j\theta_{\perp 0}r_0K_{r\perp} - ja_0K_a\right) \times \exp\left(j\theta_\perp r_0K_{r\perp} + jaK_a\right)\cos\beta_0 dK_{r\perp}dK_a \quad (22)$$

where $\Delta R_{r\perp}$ is the total component of $\Delta\vec{R}_T$ and $\Delta\vec{R}_R$ is projected along $\vec{K}_{r\perp}$ direction, whereas ΔR_r is the total component

of $\Delta\vec{R}_T$ and $\Delta\vec{R}_R$ projected along $\vec{K}_r$ direction. K_a is respected to the coordinate a, and $K_{r\perp}$ is the magnitude of $\vec{K}_{r\perp}$. In (22), $K_{r\perp}$ instead of K_θ is utilized to represent image spectrum for convenience. For $K_{r\perp}$, it has

$$K_\theta = r_0 K_{r\perp} \tag{23}$$

where K_θ is with respect to the coordinate $\theta_\perp$. For K_a and β_0 in the OEP coordinate system, it has

$$\begin{cases} \beta_0 = \frac{1}{2}\angle F_1 P_0 F_2 \\ K_a = K_r / \cos\beta_0 \end{cases} \tag{24}$$

where K_r is the magnitude of $\vec{K}_r$. The derivation of (22)–(24) is given in the appendix. According to (22), the analytical form of image spectrum in OEP can be given as

$$\begin{aligned} I\left(K_a, K_{r\perp}\right) \approx \alpha \exp\left(-j\Delta R_{r\perp} K_{r\perp} - j\Delta R_r \cos\beta_0 K_a\right) \\ \times \exp\left(-j\theta_{\perp 0} r_0 K_{r\perp} - j a_0 K_a\right)\cos\beta_0. \end{aligned} \tag{25}$$

In (25), the first exponential term is the motion error term in spectrum domain. Note that $\Delta R_{r\perp}$ and ΔR_r are originated from $\Delta\vec{R}_T$ and $\Delta\vec{R}_R$, both $\Delta R_{r\perp}$ and ΔR_r are also the functions of azimuth time t. Because (25) is the echoes represented in image spectrum domain, both $\Delta R_{r\perp}$ and ΔR_r can be also regarded as functions of K_a and $K_{r\perp}$ given as

$$\begin{cases} \Delta R_{r\perp}(t) = \Delta R_{r\perp}\left(K_a, K_{r_\perp}\right) \\ \Delta R_r(t) = \Delta R_r\left(K_a, K_{r_\perp}\right) \end{cases}. \tag{26}$$

The first exponential term of (25) contains APE and NsRCM components, both of which are induced by the unknown motion errors. In the following section, both the two components will be particularly investigated and an effective data-driven MOCO will be developed in a coherent manner.

IV. Coherent Compensation for Both APE and NsRCM

In airborne BiSAR applications, trajectory derivations usually exceed one range cell that inevitably introduces NsRCM. Thus, in the MOCO, both APE and NsRCM need to be considered. In this section, the coherence between APE and NsRCM will be revealed based on the analytical spectrum obtained in (25), then an effective data-driven MOCO will be developed in the FFBP framework.

Let $\varphi(K_a, K_{r\perp})$ be the phase error function originated from the first exponential term of (25) given as

$$\begin{aligned} \varphi_e\left(K_a, K_{r\perp}\right) \approx -\Delta R_{r\perp}\left(K_a, K_{r_\perp}\right) K_{r\perp} \\ - \Delta R_r\left(K_a, K_{r_\perp}\right)\cos\beta_0 K_a. \end{aligned} \tag{27}$$

To investigate the relationship between APE and NsRCM, (27) can be expanded in Taylor series. However, it is difficult to obtain the expressions of $\Delta R_{r\perp}(K_a, K_{r_\perp})$ and $\Delta R_r(K_a, K_{r_\perp})$ from (26), because the relationship among t, K_a, and $K_{r_\perp}$ is very complicated. To overcome this problem, an intermediate variable θ_t is introduced, which denotes the angular between $\vec{K}_\Sigma$ and $\vec{K}_r$ at azimuth time t, as shown in Fig. 1. Then, $\Delta R_{r\perp}$ and ΔR_r in (26) and (27) can be also regarded as functions of θ_t

$$\begin{cases} \Delta R_{r\perp}\left(K_a, K_{r_\perp}\right) = \Delta R_{r\perp}\left(\theta_t\right) \\ \Delta R_r\left(K_a, K_{r_\perp}\right) = \Delta R_r\left(\theta_t\right) \end{cases}. \tag{28}$$

As shown in Fig. 1, the relationship among θ_t, K_a, and $K_{r_\perp}$ can be readily achieved according to the geometry given as

$$\theta_t = \arctan\frac{K_{r\perp}}{K_r}. \tag{29}$$

By using (24), (29) can be rewritten as

$$\theta_t = \arctan\frac{K_{r\perp}}{K_a\cos\beta_0}. \tag{30}$$

By substituting (30) into (28), it has

$$\begin{cases} \Delta R_{r\perp}\left(K_a, K_{r_\perp}\right) = \Delta R_{r\perp}\left(\arctan\frac{K_{r\perp}}{K_a\cos\beta_0}\right) \\ \Delta R_r\left(K_a, K_{r_\perp}\right) = \Delta R_r\left(\arctan\frac{K_{r\perp}}{K_a\cos\beta_0}\right) \end{cases}. \tag{31}$$

With (31), the expressions of $\Delta R_{r\perp}(K_a, K_{r_\perp})$ and $\Delta R_r(K_a, K_{r_\perp})$ have been achieved and Taylor expansion can be applied to (27) to investigate the coherence between APE and NsRCM in image spectrum domain. Let K_{a0} be the center of K_a, by applying first-order Taylor expansion with respect to $K_a = K_{a0}$, (27) can be approximated as

$$\varphi_e\left(K_a, K_{r\perp}\right) \approx \varphi_0\left(K_{a0}, K_{r\perp}\right) + \varphi_1\left(K_{a0}, K_{r\perp}\right)\Delta K_a \tag{32}$$

where $\Delta K_a = K_a - K_{a0}$. In (32), $\varphi_0(K_{a0}, K_{r\perp})$ and $\varphi_1(K_{a0}, K_{r\perp})$ can be given as

$$\begin{aligned} \varphi_0\left(K_{a0}, K_{r\perp}\right) &= \varphi_e\left(K_a, K_{r\perp}\right)\Big|_{K_a = K_{a0}} \\ &= -\Delta R_r\left(\arctan\frac{K_{r\perp}}{K_{a0}\cos\beta_0}\right)\cos\beta_0 K_{a0} \\ &\quad - \Delta R_{r\perp}\left(\arctan\frac{K_{r\perp}}{K_{a0}\cos\beta_0}\right) K_{r\perp} \end{aligned} \tag{33}$$

and

$$\begin{aligned} \varphi_1\left(K_{a0}, K_{r\perp}\right) &= \frac{\partial\varphi_e\left(K_a, K_{r\perp}\right)}{\partial K_a}\Big|_{K_a = K_{a0}} \\ &= \Delta R_r'\left(\arctan\frac{K_{r\perp}}{K_{a0}\cos\beta_0}\right) \\ &\quad \times \frac{1}{\sqrt{\left(\frac{K_{r\perp}}{K_{a0}\cos\beta_0}\right)^2 + 1}} \times \frac{K_{r\perp}}{K_{a0}} \\ &\quad - \Delta R_r\left(\arctan\frac{K_{r\perp}}{K_{a0}\cos\beta_0}\right)\cos\beta_0 \\ &\quad + \Delta R_{r\perp}{}'\left(\arctan\frac{K_{r\perp}}{K_{a0}\cos\beta_0}\right) \\ &\quad \times \frac{1}{\sqrt{\left(\frac{K_{r\perp}}{K_{a0}\cos\beta_0}\right)^2 + 1}} \times \frac{K_{r\perp}^2}{K_{a0}^2\cos\beta_0} \end{aligned} \tag{34}$$

where the notation "′" denotes the first-order derivation with respect to K_a. In (32), the first term $\varphi_0(K_{a0}, K_{r\perp})$ is the APE term, which is independent of ΔK_a. Before NsRCM correction, $\varphi_0(K_{a0}, K_{r\perp})$ can be coarsely estimated by using the conventional autofocusing techniques, e.g., PGA [29] and minimum entropy autofocusing [30], and the coarsely estimated values are usually accurate enough for NsRCM correction [31], [32].

Let us consider the second term $\varphi_1(K_{a0}, K_{r\perp})\Delta K_a$ of (32), which denotes the NsRCM component. As shown in (34), the exactly values of $\Delta R_{r\perp}$ and ΔR_r cannot be obtained individually due to the fact that the unknown motion errors from both transmitter and receiver are coupled with each other. Thus, we need to investigate the coherence between APE and NsRCM and use the coarsely estimated $\varphi_0(K_{a0}, K_{r\perp})$ to achieve the unknown NsRCM. Here, we split $\varphi_1(K_{a0}, K_{r\perp})$ of (34) into two parts as

$$\varphi_1\left(K_{a0}, K_{r\perp}\right) = \varphi_{\text{RCM1}}\left(K_{a0}, K_{r\perp}\right) + \varphi_{\text{RCM2}}\left(K_{a0}, K_{r\perp}\right) \tag{35}$$

where

$$\begin{aligned}\varphi_{\text{RCM1}}\left(K_{a0}, K_{r\perp}\right) = &-\Delta R_r\left(\arctan\frac{K_{r\perp}}{K_{a0}\cos\beta_0}\right)\cos\beta_0 \\ &- \Delta R_{r\perp}\left(\arctan\frac{K_{r\perp}}{K_{a0}\cos\beta_0}\right)\frac{K_{r\perp}}{K_{a0}}\end{aligned} \tag{36}$$

and

$$\begin{aligned}\varphi_{\text{RCM2}}\left(K_{a0}, K_{r\perp}\right) = &\Delta R_r'\left(\arctan\frac{K_{r\perp}}{K_{a0}\cos\beta_0}\right) \\ &\times \frac{1}{\sqrt{\left(\frac{K_{r\perp}}{K_{a0}\cos\beta_0}\right)^2 + 1}} \times \frac{K_{r\perp}}{K_{a0}} \\ &+ \Delta R_{r\perp}{}'\left(\arctan\frac{K_{r\perp}}{K_{a0}\cos\beta_0}\right) \\ &\times \frac{1}{\sqrt{\left(\frac{K_{r\perp}}{K_{a0}\cos\beta_0}\right)^2 + 1}} \times \frac{K_{r\perp}^2}{K_{a0}^2\cos\beta_0} \\ &+ \Delta R_{r\perp}\left(\arctan\frac{K_{r\perp}}{K_{a0}\cos\beta_0}\right)\frac{K_{r\perp}}{K_{a0}}.\end{aligned} \tag{37}$$

By observing (36), it can be noted that the first term of (35) is linearly proportional to the APE and the φ_{RCM1} component of (35) can be represented by the APE as

$$\varphi_{\text{RCM1}}\left(K_{a0}, K_{r\perp}\right) = \frac{1}{K_{a0}}\varphi_0\left(K_{a0}, K_{r\perp}\right). \tag{38}$$

The second term of (35) is linearly proportional to the first-derivation of APE and the φ_{RCM2} component of (35) can be represented by the APE as

$$\varphi_{\text{RCM2}}\left(K_{a0}, K_{r\perp}\right) = -\frac{\partial\varphi_0\left(K_a, K_{r\perp}\right)}{\partial K_{r\perp}}\frac{K_{r\perp}}{K_{a0}}. \tag{39}$$

The φ_{RCM2} component can be also referred to as residual NsRCM. It should be emphasized that the residual NsRCM is particularly introduced by projecting the echoes onto the polar coordinates system in the fast TDA, which is quite different from most FDAs. In most FDAs for MOCO, only the φ_{RCM1} component of (35) needs to be considered. However, in the fast TDA for MOCO, the residual NsRCM needs to be particularly estimated and compensated. So far, the coherence between APE and NsRCM is perfectly revealed. Based on the coherence, the NsRCM correction can be exactly correctly by the coarsely estimated APE. By utilizing the coarsely estimated APE $\varphi_0(K_{a0}, K_{r\perp})$ and according to (38) and (39), the NsRCM correction can be given as

$$H_1\left(K_{a0}, K_{r\perp}\right) = \left[-\frac{1}{K_{a0}}\varphi_0\left(K_{a0}, K_{r\perp}\right)\right]\Delta K_a \tag{40}$$

and

$$H_2\left(K_{a0}, K_{r\perp}\right) = \left[\frac{\partial\varphi_0\left(K_a, K_{r\perp}\right)}{\partial K_{r\perp}}\frac{K_{r\perp}}{K_{a0}}\right]\Delta K_a. \tag{41}$$

By adding (40) and (41) to (32), the NsRCM components can be exactly removed. After NsRCM correction, the autofocusing process is applied again for fine APE estimation and compensation to achieve a well – focused image.

V. Processing Procedure

The processing procedures of data-driven MOCO in an FFBP framework is summarized in Fig. 2, which includes main three steps. Details are given in the following.

Step 1. FFBP processing: At first step, the raw echoed signal collected in the BiSAR mode will be preprocessed, e.g., range compressing or range deramp processing, and $S(t, K_r)$ can be obtained, which is also described in (6). Then, the preprocessed signal $S(t, K_r)$ is processed by FFBP for SAR imagery. If available, the airborne INS/GPS information can be readily incorporated into FFBP for preliminary MOCO. If the INS/GPS information is not accurate enough or the INS/GPS information is unavailable, the proposed algorithm can be used to compensate for the unknown motion error in a data-driven manner. To achieve a higher computational efficiency, the preprocessed signal $S(t, K_r)$ is projected onto the OEP grid and image $i(a, \theta_\perp)$ is obtained, described in (22). Then, $i(a, \theta_\perp)$ is transformed into the range-compressed azimuth-spectrum domain by utilizing azimuth fast fourier transform (FFT) and $I(a, K_{r\perp})$ is obtained.

Step 2. Coherent MOCO for both APE and NsRCM: After the image is transformed into the range-compressed azimuth-spectrum domain, i.e., $I(a, K_{r\perp})$ domain, for weighted PGA (WPGA) [29] processing. Because at this step, the NsRCM problem will adversely affect the accuracy of APE estimation, and only coarse APE can be obtained. But the coarsely obtained APE $\hat{\varphi}_0(K_{a0}, K_{r\perp})$ is accurate enough for NsRCM correction. Note that, for MOCO in the fast TDA, the residual NsRCM needs to be particularly considered. According to (40) and (41), the correction functions for NsRCM compensation can be easily obtained by using the coherence between APE and NsRCM. With $\hat{\varphi}_0(K_{a0}, K_{r\perp})$, $H_1(K_{a0}, K_{r\perp})$, and $H_2(K_{a0}, K_{r\perp})$, the NsRCM correction as well as coarse APE compensation can be subsequently performed.

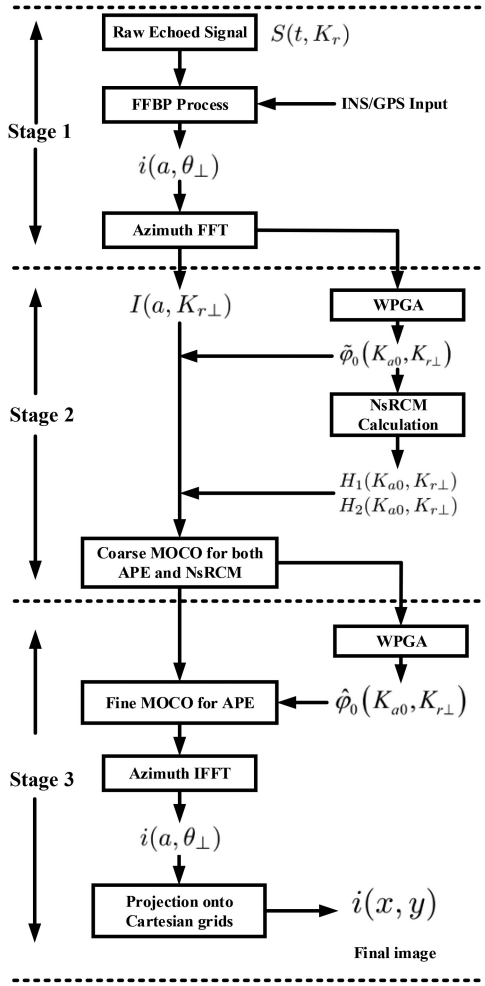

Fig. 2. Processing procedures of the proposed algorithm.

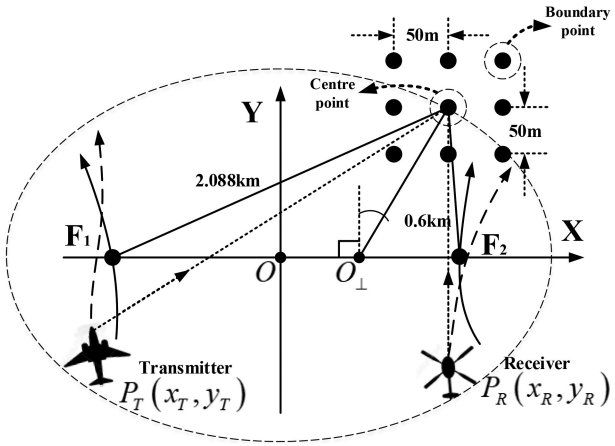

Fig. 3. Geometry and point location in the simulation.

TABLE I
BISAR PARAMETERS IN SIMULATION EXPERIMENT

Wave Band	Ku
Bandwidth	200 MHz
PRF	1000 Hz
Base line	2000 m
Range R_R	600 m
Range R_T	2088 m
Velocity vector V_T	(0,80) m/s
Acceleration vector a_T	(-0.1,0.2) m/s^2
Velocity vector V_R	(-20,60) m/s
Acceleration vector a_R	(0.2,-0.3) m/s^2

Step 3: After the NsRCM being corrected, WPGA is performed again for fine APE estimation and the residual APE can be effectively removed. The fine estimated APE is denoted as $\tilde{\varphi}_0(K_{a0}, K_{r\perp})$, as shown in Fig. 2. Finally, an azimuth inverse fast fourier transform (IFFT) is implemented to achieve a well – focused image $i(a, \theta_\perp)$. As the proposed algorithm is performed in OEP grids $(a, \theta_\perp)$, the image should be projected into the Cartesian coordinates and the image $i(x, y)$ is obtained.

VI. Simulation and Raw Data Experiment

In this section, both simulations and raw data experiments for the general BiSAR process are presented and analyzed to evaluate the performance of the proposed algorithm.

A. Simulation Experiments

In the simulation experiments, the geometries of simulation are in accordance with Fig. 3, and the parameters are according to Table I, where R_R is the range from F_2 to the center scatterer, whereas R_T is the range from F_1 to the center scatterer. The ideal trajectories of both transmitter and receiver can be given by $(x_T, y_T) = V_T t + (1/2)a_T t^2$ and $(x_R, y_R) = V_R t + (1/2)a_R t^2$, respectively. In the simulation, motion errors in both platforms along both *X* and *Y* directions are assumed. Fig. 4 shows the motion errors of transmitter and receiver platforms in *X* and *Y* directions. The algorithms for both simulation experiments and raw data experiments are programmed on a MATLAB platform and windows 10 system running on a PC with i7-9700 CPU and 32-GB RAM without parallel processing. The full aperture is 4 s. In total, nine-point scatterers are simulated in the observing scene, and each of them are set with a uniform spacing of 50 m, as shown in Fig. 3.

To improve the focusing quality, a WPGA technique is utilized for APE estimation in the MOCO. By implementing the processing steps given in Section II, the APE as well as NsRCM can be obtained. In the FFBP process for MOCO, the residual NsRCM φ_{RCM2} needs to be particularly considered. The NsRCM correction for center point is investigated in Fig. 5. Fig. 5(a) shows the NsRCM of the center point without any correction, which shows that the energy spreads into several range cells. Fig. 5(b) presents the results by using the conventional NsRCM correction, i.e., only the $\varphi_{\text{RCM1}}(K_{a0}, K_{r\perp})$ component in (35) is corrected but the residual NsRCM φ_{RCM2} is not corrected. It is seen that the NsRCM problem is even worse due to the improper ignorance of the large residual NsRCM. Fig. 5(c) presents the results after residual NsRCM being corrected. It can be seen that the range cell migration has been desirably removed, which validates the effectiveness of the proposed coherent MOCO for NsRCM compensation.

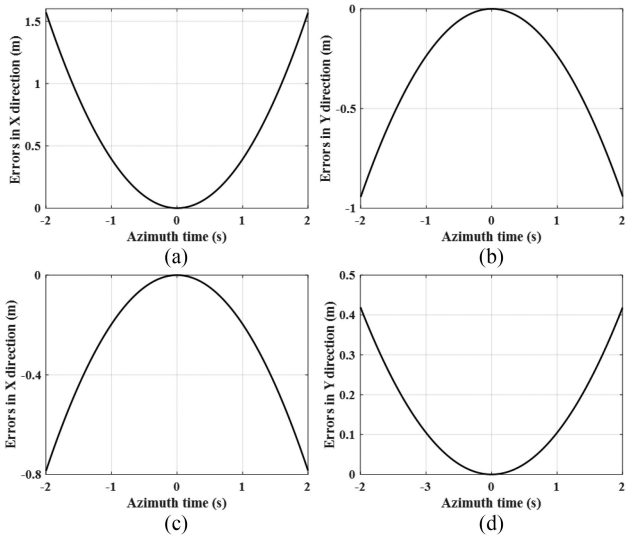

Fig. 4. Motion errors of the transmitter and receiver in two dimensions. (a) Error along the *X* direction of the transmitter. (b) Errors along the *Y* direction of the transmitter. (c) Error along the *X* direction of the receiver. (d) Errors along the *Y* direction of the receiver.

To evaluate the performance of the proposed algorithm, the focusing quality of both the center point and the boundary point described in Fig. 3 are particularly analyzed. The total time consumption by the proposed algorithm is 6.7 min, which is much faster than 107.1 min processed by the direct BP algorithm. Fig. 6 shows the focusing results of center and boundary points without any MOCO, and it is seen that the focusing quality degraded very obviously. After both APE and NsRCM are compensated in the simulated data, the point scatterers are refocused with good quality, as shown in Fig. 7. To further demonstrate the advantages of the proposed algorithm, a current fast BP algorithm integrated with data-driven MOCO from [23] is employed here for comparison. Due to the fact that the algorithm of [23] cannot compensate for the NsRCM in the FFBP process, it cannot achieve promising results. Fig. 8 compares the angular responses from both algorithms for boundary point focusing. The dashed line denotes the results from the algorithm of [23] and the solid line is the results from the proposed algorithm. From the comparison, it is seen that the proposed algorithm can achieve higher performance. By using the proposed algorithm, the obtained angular resolution is about 0.32 m and the range resolution is about 0.77 m, which are very close to the theoretic resolution (angular 0.30 m, range 0.75 m), which demonstrates the performance advantages of the propose algorithm.

B. Raw Data Experiment

In this section, the raw data experiments are provided and analyzed to further evaluate the performance of the proposed method. The raw data is acquired from a one-stationary airborne BiSAR test bed, as shown in Fig. 9. In the experiment, the transmitter is mounted on an aircraft with a velocity about 65 m/s. The transmitter is operating at Ku band with a bandwidth of 80 MHz. The transmitter is working on side-looking mode with a small squint angle. The receiver is fixed on a hill near the illuminating scenario. The image area is about 3.5 km $\times$ 1.1 km (*X* direction $\times$ *Y* direction). Because the digital elevation model (DEM) data are unavailable, it is assumed that the illuminated scene is on a flat plane. The FFBP algorithm as well as the proposed date-driven MOCO is running on the same platform mentioned in simulation section.

Due to the fact that the INS/GPS information is not accurate enough for SAR focusing, data-driven MOCO is utilized in the FFBP process. Because the BiSAR test bed operates in the mode with wide swath, the influence of phase error varying in range direction is considered and the method described in [18] is utilized for the range-variant phase compensation. The estimated APE and NsRCM are particularly analyzed, as shown Fig. 10. In Fig. 10(b), the solid curve denotes the first part of NsRCM and the dashed line denotes the residual NsRCM, both of which are obtained from the estimated APE. From Fig. 10(b), it is seen that the NsRCM exceeds one half of the range cell (1.5 m) and will adversely affect the APE estimation and the quality in focusing. So that, it is necessary to correct the NsRCM in the MOCO. The NsRCM correction for prominent scatterer 1 (described in Fig. 13) in the scenario is investigated in Fig. 11. Fig. 11(a) shows the NsRCM of the prominent scatterer 1 without any correction, which shows that the energy spreads into several range cells that will bring difficulties for fine APE estimation and compensation. Fig. 11(b) presents the results by using the conventional NsRCM correction, i.e., only the $\varphi_{\mathrm{RCM1}}(K_{a0}, K_{r\perp})$ component in (35) is corrected but the residual NsRCM $\varphi_{\mathrm{RCM2}}(K_{a0}, K_{r\perp})$ is not considered. It is seen that the NsRCM cannot be exactly corrected due to the improper ignorance of the large residual NsRCM shown in Fig. 10(b). Fig. 11(c) presents the results after both terms of NsRCM described in (35) being corrected. It is seen that the range cell migration has been desirably removed, which validates the effectiveness of the proposed coherent MOCO for NsRCM compensation.

For full aperture data processing, the total time consumption of the direct BP process is about 251 min. By utilizing FFBP without MOCO, the total time consumption is about 14.7 min, which is much faster than the direct BP process. By utilizing FFBP integrated with the proposed MOCO algorithm, the total time consumption of FFBP integrated with the proposed MOCO is about 15.2 min, which shows that the proposed MOCO algorithm will not increase much computational burden to the FFBP process. The final images are shown in Fig. 12 with the image size is about 3.4 $\times$ 1.1 km (*X* direction $\times$ *Y* direction). Fig. 12(a) shows the focusing result without any MOCO and it is seen that the focusing quality is degraded seriously due to the unexpected motion error, and the entropy of image is 11.411. To further demonstrate the advantages of the proposed algorithm, the algorithm of [23] is employed here for comparison. Fig. 12(b) is the focusing results from the algorithm of [23]. Due to the fact that the algorithm of [23] cannot compensate for the NsRCM in the FFBP process, it cannot achieve promising results. The entropy of the SAR image obtained by algorithm of [23] is 10.916. Fig. 12(c) is the results from the proposed algorithm and it is seen that the focusing quality improved obviously and the image entropy decreased to 10.892. Fig. 13 presents the

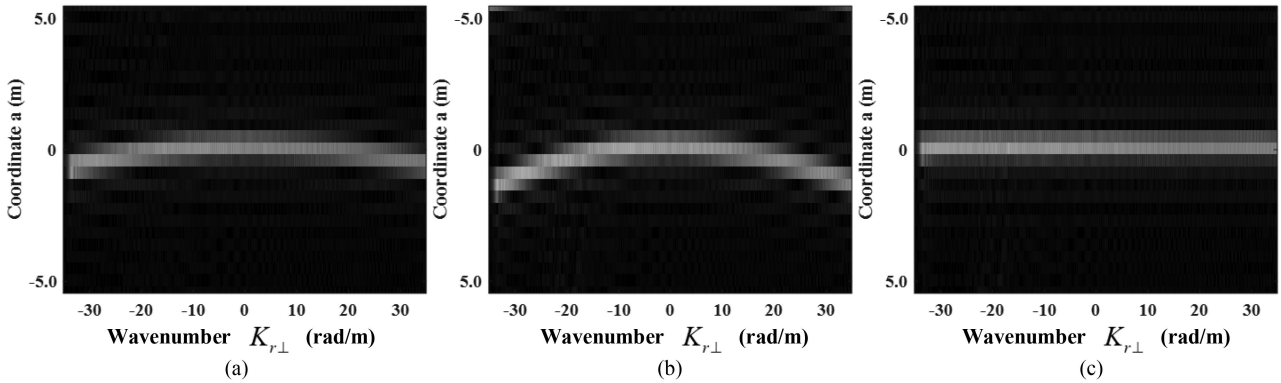

Fig. 5. NsRCM correction in the simulation experiment. (a) Without any NsRCM correction. (b) Conventional NsRCM correction without considering residual NsRCM. (c) NsRCM correction by the proposed algorithm.

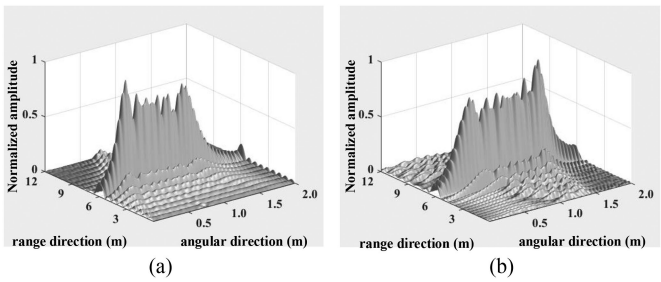

Fig. 6. Focusing results without any MOCO. (a) Center point. (b) Boundary point.

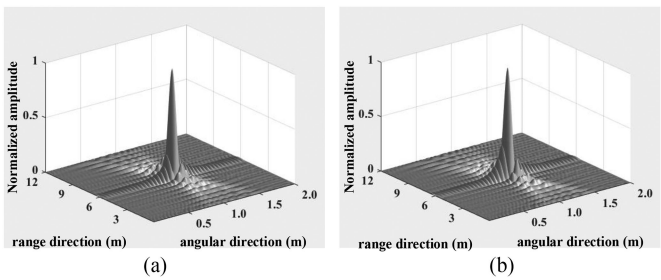

Fig. 7. Focusing results by using the proposed MOCO. (a) Center point. (b) Boundary point.

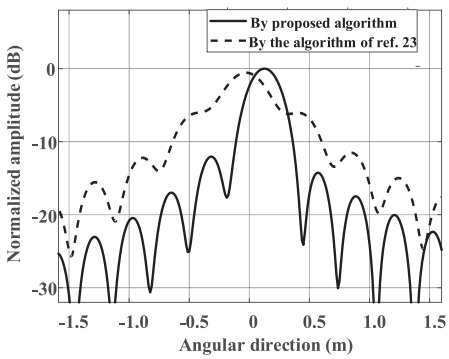

Fig. 8. Responses in angular direction of boundary point. The dashed curve denotes the results from the algorithm of [23] and the solid curve denotes the results from the proposed algorithm.

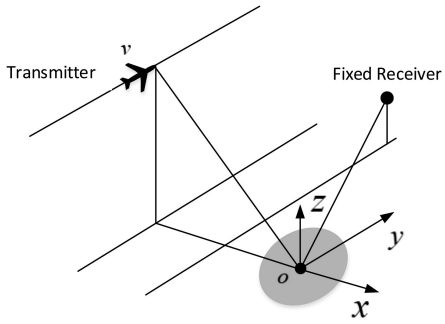

Fig. 9. Experimental geometry of one-stationary BiSAR.

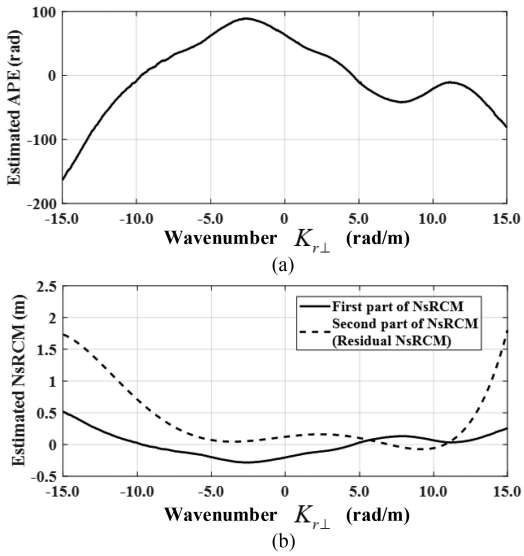

Fig. 10. Estimated APE and NsRCM of raw data experiment. (a) Esimated APE. (b) Estimated NsRCM.

zoomed images, and it is shown that the buildings as well as the roads can be clearly distinguished in the SAR image. Then, the azimuth responses of two prominent scatterers are particularly investigated, as shown in Fig. 14. The obtained resolution in azimuth is about 0.38 m. The dashed line is the results from

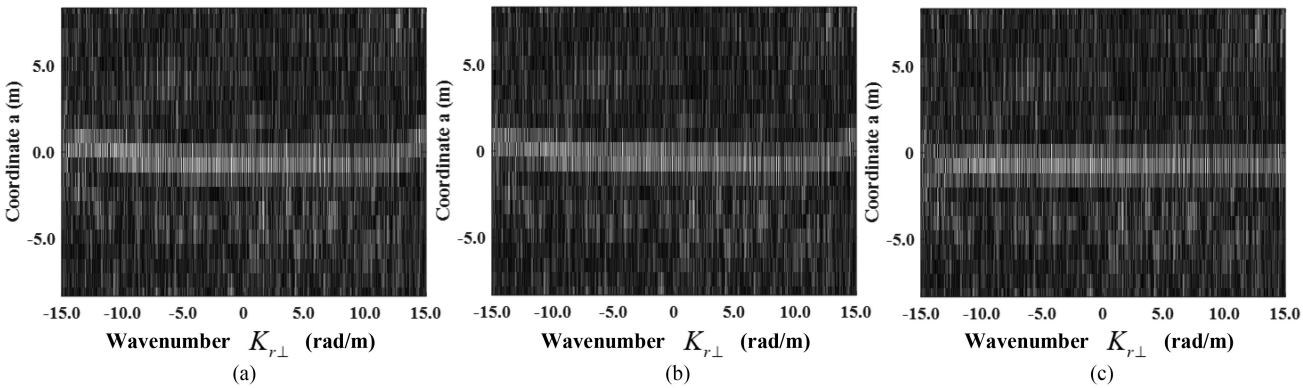

Fig. 11. NsRCM correction in the raw data experiment. (a) Without any NsRCM correction. (b) Conventional NsRCM correction without considering residual NsRCM. (c) NsRCM correction by the proposal.

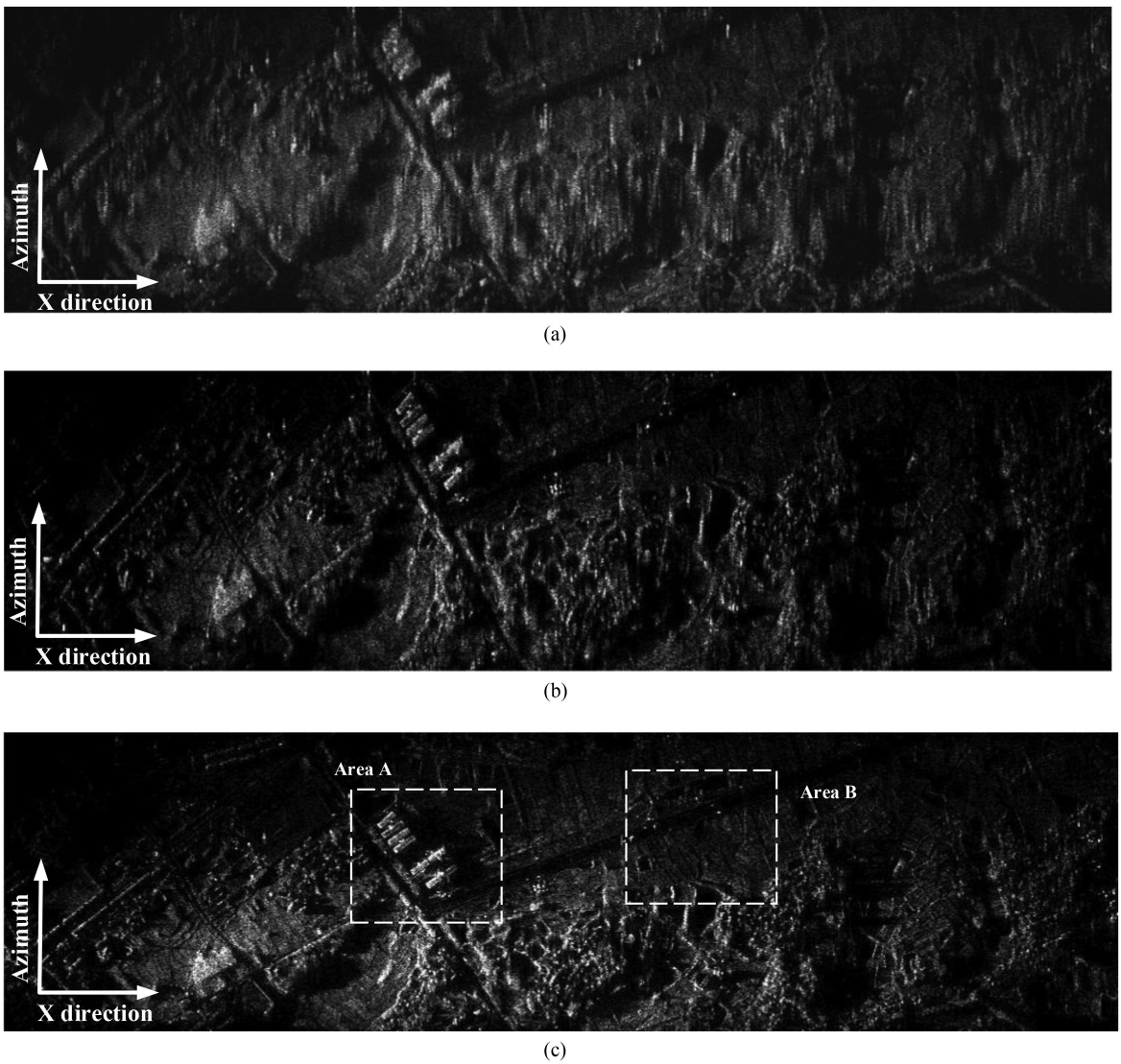

Fig. 12. Final image from one-stationary BiSAR test bed. (a) Results from FFBP without data-driven MOCO. (b) Results from the algorithm of Ref. [23]. (c) Results from FFBP integrated with the proposed MOCO.

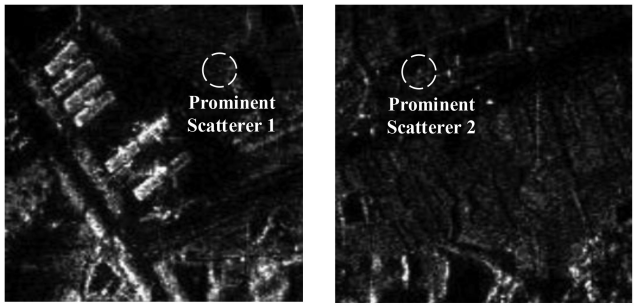

Fig. 13. Zoomed images and prominent scatterers. (a) Zoomed image of area A. (b) Zoomed image of area B.

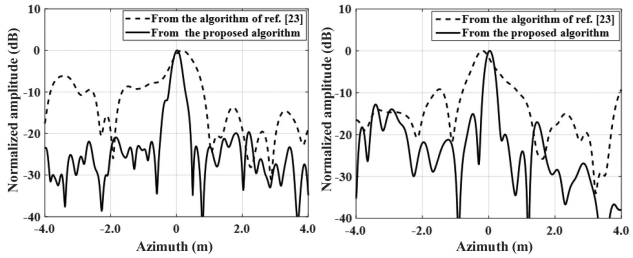

Fig. 14. Azimuth responses of the prominent scatterers. The obtained resolution in azimuth is about 0.38 m. (a) Azimuth responses of prominent scatterer 1. (b) Azimuth responses of prominent scatterer 2.

the algorithm of [23], whereas the solid denotes the results from the proposed algorithm. From the comparison, it is seen that the proposed algorithm achieved better performance, which demonstrates the higher performance of the proposed algorithm.

VII. Conclusion

In this article, a data-driven MOCO is developed under an FFBP framework for a general BiSAR process. The coherence between APE and NsRCM is revealed based on which both APE and NsRCM can be exactly estimated and compensated in a coherent manner. By utilizing the proposed algorithm, the focusing quality of BiSAR image is improved very obviously, which validates the performance of the proposal.

Appendix A

In this appendix, the derivation for (22) is given in detail. Fig. 15 shows the geometric relationship in the OEP system with motion errors. In Fig. 15, the image grid $P(x,y)$ in (7) and (8) is represented as $P(a,\theta_\perp)$, where a and $\theta_\perp$ are the new coordinates in the OEP system. According to Fig. 15, the range vectors $\vec{R}_0$ and $\vec{R}$ can be represented by $\vec{OP}_0$ and $\vec{OP}$. Both $\vec{R}_0$ and $\vec{R}$ can be decomposed along $K_{r\perp}$ and $K_{r\perp}$ directions given as

$$\begin{cases} \vec{R}_0 = \vec{ON} + \vec{NP}_0 \\ \vec{R} = \vec{OL} + \vec{LP} \end{cases}. \tag{A1}$$

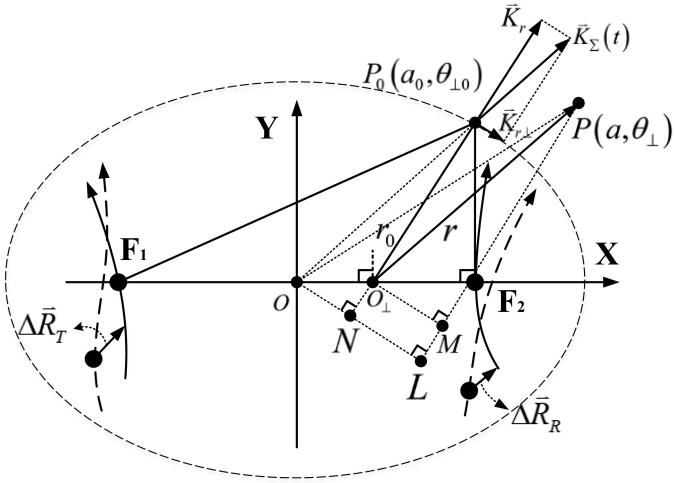

Fig. 15. Geometry relationship in the OEP system.

In (19), the error vectors can be decomposed along $K_{r\perp}$ and $K_{r\perp}$ directions given as

$$\begin{cases} \Delta\vec{R}_T = \Delta\vec{R}_{Tr\perp} + \Delta\vec{R}_{Tr} \\ \Delta\vec{R}_R = \Delta\vec{R}_{Rr\perp} + \Delta\vec{R}_{Rr} \end{cases}. \tag{A2}$$

The wavenumbers in (19) decomposed along $K_{r\perp}$ and K_r directions can be given as

$$\begin{cases} \vec{K}_T = \vec{K}_{Tr\perp} + \vec{K}_{Tr} \\ \vec{K}_R = \vec{K}_{Rr\perp} + \vec{K}_{Rr} \\ \vec{K}_\Sigma = \vec{K}_{\Sigma r\perp} + \vec{K}_{\Sigma r} \end{cases} \tag{A3}$$

By substituting (A1)–(A3) into (19), it has

$$\begin{aligned} i(a,\theta_\perp) = \int\int & \exp\left(-j\Delta\vec{R}_{Tr\perp}\cdot\vec{K}_{Tr\perp} - j\Delta\vec{R}_{Tr}\cdot\vec{K}_{Tr}\right) \\ & \times \exp\left(-j\Delta\vec{R}_{Rr\perp}\cdot\vec{K}_{Rr\perp} - j\Delta\vec{R}_{Rr}\cdot\vec{K}_{Rr}\right) \\ & \times \exp\left[-j\left(\vec{ON} - \vec{OL}\right)\cdot\vec{K}_{\Sigma r\perp}\right] \\ & \times \exp\left[-j\left(\vec{NP}_0 - \vec{LP}\right)\cdot\vec{K}_{\Sigma r}\right]\alpha|J|dK_{r\perp}dK_r. \end{aligned} \tag{A4}$$

The wavenumbers $K_{Tr\perp}$, $K_{Rr\perp}$, and $K_{\Sigma r\perp}$ have the same direction, and let $K_{r\perp}$ be the intersection of $K_{Tr\perp}$, $K_{Rr\perp}$, and $K_{\Sigma r\perp}$. Similarly, the wavenumbers K_{Tr}, K_{Rr}, and $K_{\Sigma r}$ have the same direction, and let K_r be the intersection of K_{Tr}, K_{Rr}, and $K_{\Sigma r}$. Then, it has

$$\begin{cases} \vec{K}_{r\perp} = \vec{K}_{Tr\perp} \cap \vec{K}_{Rr\perp} \cap \vec{K}_{\Sigma r\perp} \\ \vec{K}_r = \vec{K}_{Tr} \cap \vec{K}_{Rr} \cap \vec{K}_{\Sigma r} \end{cases}. \tag{A5}$$

Then, we introduce a pair of error vectors $\Delta\vec{R}_{r\perp}$ and $\Delta\vec{R}_r$, where $\Delta\vec{R}_{r\perp}$ denotes the motion errors of both transmitter and receiver projected along $\vec{K}_{r\perp}$ direction, whereas $\Delta\vec{R}_r$ denotes the motion errors of both transmitter and receiver projected along

$\vec{K}_r$ direction given as

$$\begin{cases} \Delta\vec{R}_{r\perp} = \Delta\vec{R}_{Tr\perp} + \Delta\vec{R}_{Tr\perp} \\ \Delta\vec{R}_r = \Delta\vec{R}_{Tr} + \Delta\vec{R}_{Rr} \end{cases}. \tag{A6}$$

Let r_0 be the range from $O_\perp$ to P_0 and r be the range from $O_\perp$ to P. According to the geometry in Fig. 15, it has

$$\begin{cases} r\sin(\theta_{\perp 0} - \theta_\perp) = -\left|\vec{ON} - \vec{OL}\right| \\ r_0 - r\cos(\theta_{\perp 0} - \theta_\perp) = -\left|\vec{NP}_0 - \vec{LP}\right| \end{cases}. \tag{A7}$$

By substituting (A5)–(A7) into (A4) and using simple manipulations, it obtains

$$\begin{aligned} i(a,\theta_\perp) \approx & \int\int \alpha\left|J\right| \exp\left(-j\Delta R_{r\perp}K_{r\perp} - j\Delta R_r K_r\right) \\ & \times \exp\left(-j[r\sin(\theta_{\perp 0} - \theta_\perp)]K_{r\perp}\right) \\ & \times \exp\left\{-j\left[r_0 - r\cos(\theta_{\perp 0} - \theta_\perp)\right]\cdot K_r\right\} dK_{r\perp}dK_r \end{aligned} \tag{A8}$$

where $|J|$ is the Jacobian determinant [28]. Generally in SAR processing, we mainly concern the phase modulation and the change of $|J|$ can be ignored. In our analyses, $|J|$ is assumed to be a constant in the derivation.

Let us introduce the principle of stationary phase (POSP) [33] to investigate (A8) and let $\varphi(K_{r\perp}, K_r)$ be the phase function of (A8). According to POSP, the integral in (A8) is valid when the following requirements are satisfied:

$$\frac{\partial\varphi(K_{r\perp}, K_r)}{\partial K_{r\perp}} = 0 \quad \text{and} \quad \frac{\partial\varphi(K_{r\perp}, K_r)}{\partial K_r} = 0. \tag{A9}$$

Here, we need to solve (A9) to investigate (A8). Note that, the first exponential term of (A8) is from the motion errors. Generally the motion errors are small and the contribution of the first exponential term to the solution can be neglected. By solving (A9), it obtains

$$\begin{cases} r\sin(\theta_{\perp 0} - \theta_\perp) \approx 0 \\ r_0 - r\cos(\theta_{\perp 0} - \theta_\perp) \approx 0 \end{cases}. \tag{A10}$$

Based on (A10), it obtains

$$\theta_{\perp 0} - \theta_\perp \approx 0 \quad \text{and} \quad r_0 - r \approx 0. \tag{A11}$$

By observing (A11), the POSP explains the fact that the contribution to the integral (A8) is mainly from the energy very close to $(r_0, \theta_{\perp 0})$. Meanwhile, in the image, as the grids away from $(r_0, \theta_{\perp 0})$, the energy of P_0 decays very rapidly. Therefore, we only need to concern the grids close to $(r_0, \theta_{\perp 0})$ for focusing P_0. The POSP also explains why a point can be focused in a "sinc" sharp onto the image after the BP process. According to (A11), the following approximations can be used for SAR analyses:

$$\begin{cases} \sin(\theta_{\perp 0} - \theta_\perp) \approx \theta_{\perp 0} - \theta_\perp \\ r_0 - r\cos(\theta_{\perp 0} - \theta_\perp) \approx r_0 - r \end{cases}. \tag{A12}$$

By substituting (A12) into (A8), it has

$$\begin{aligned} i(a,\theta_\perp) \approx & \int\int \alpha\exp\left(-j\Delta R_{r\perp}K_{r\perp} - j\Delta R_r K_r\right) \\ & \times \exp\left[-jr(\theta_{\perp 0} - \theta_\perp)\cdot K_{r\perp}\right] \\ & \times \exp\left[-j(r_0 - r)\cdot K_r\right] dK_{r\perp}dK_r. \end{aligned} \tag{A13}$$

Because $r_0 \approx r$ and $\theta_{\perp 0} \approx \theta_\perp$ for the integral, based on the geometrical property of ellipse, the following approximation can be obtained as:

$$r_0 - r \approx \frac{1}{\cos\beta_0}(a_0 - a). \tag{A14}$$

where

$$\beta_0 = \frac{1}{2}\angle F_1P_0F_2. \tag{A15}$$

By substituting (A14) into (A13), and let $K_r = K_a\cos\beta_0$ and $rK_{r\perp} \approx r_0K_{r\perp}$, (22) can be obtained.

ACKNOWLEDGMENT

The authors would like to thank the anonymous reviewers for their valuable comments to improve the quality of this article.

REFERENCES

[1] A. Moreira, P. Prats-Iraola, M. Younis, G. Krieger, I. Hajnsek, and K. P. Papathanassiou, "A tutorial on synthetic aperture radar," *IEEE Geosci. Remote Sens. Mag.*, vol. 1, no. 1, pp. 6–43, Mar. 2013.

[2] R. Wang and Y. Deng, *Bistatic SAR System and Signal Processing Technology*. New York, NY, USA: Springer, 2018.

[3] J. Yang *et al.*, "A first experiment of airborne bistatic forward-looking SAR-preliminary results," in *Proc. IEEE Int. Geosci. Remote Sens. Symp.*, 2013, pp. 4202–4204.

[4] J. Wu, Z. Sun, H. An, J. Qu, and J. Yang, "Azimuth signal multichannel reconstruction and channel configuration design for geosynchronous spaceborne–airborne bistatic SAR," *IEEE Trans. Geosci. Remote Sens.*, vol. 57, no. 4, pp. 1861–1872, Apr. 2019.

[5] H. Mei, Y. Li, M. Xing, Y. Quan, and C. Wu, "A frequency-domain imaging algorithm for translational variant bistatic forward-looking SAR," *IEEE Trans. Geosci. Remote Sens.*, vol. 58, no. 3, pp. 1502–1515, Mar. 2020.

[6] O. Loffeld, H. Nies, V. Peters, and S. Knedlik, "Models and useful relations for bistatic SAR processing," *IEEE Trans. Geosci. Remote Sens.*, vol. 42, no. 10, pp. 2031–2038, Oct. 2004.

[7] T. Xiong, M. Xing, X.-G. Xia, and Z. Bao, "New applications of Omega-K algorithm for SAR data processing using effective wavelength at high squint," *IEEE Trans. Geosci. Remote Sens.*, vol. 51, no. 5, pp. 3156–3169, May 2013.

[8] M. Bao, M. D. Xing, and Y. C. Li, "Chirp scaling algorithm for geo SAR based on fourth-order range equation," *Electron. Lett.*, vol. 48, no. 1, pp. 41–42, 2012.

[9] W. Pu, W. Li, J. Wu, Y. Huang, J. Yang, and H. Yang, "An azimuth-variant autofocus scheme of bistatic forward-looking synthetic aperture radar," *IEEE Geosci. Remote Sens. Lett.*, vol. 14, no. 5, pp. 689–693, May 2017.

[10] L. Zhao, L. Wang, G. Bi, and L. Yang, "An autofocus technique for high-resolution inverse synthetic aperture radar imagery," *IEEE Trans. Geosci. Remote Sens.*, vol. 52, no. 10, pp. 6392–6403, Oct. 2014.

[11] M. Rodriguez-Cassola, P. Prats, G. Krieger, and A. Moreira, "Efficient time-domain image formation with precise topography accommodation for general bistatic SAR configurations," *IEEE Trans. Aerosp. Electron. Syst.*, vol. 47, no. 4, pp. 2949–2966, Oct. 2011.

[12] J. L. Bauck and W. K. Jenkins, "Convolution-backprojection image reconstruction for bistatic synthetic aperture radar," in *Proc. IEEE Int. Symp. Circuits Syst.*, 1989, pp. 1512–1515.

[13] V. T. Vu and M. I. Pettersson, "Nyquist sampling requirements for polar grids in bistatic time-domain algorithms," *IEEE Trans. Signal Process.*, vol. 63, no. 2, pp. 457–465, Jan. 2015.

[14] A. F. Yegulalp, "Fast backprojection algorithm for synthetic aperture radar," in *Proc. IEEE Radar Conf., Rec.*, 1999, pp. 60–65.

[15] L. M. H. Ulander, H. Hellsten, and G. Stenstrom, "Synthetic-aperture radar processing using fast factorized back-projection," *IEEE Trans. Aerosp. Electron. Syst.*, vol. 39, no. 3, pp. 760–776, Jul. 2003.

[16] L. Yang, P. Li, S. Zhang, L. Zhao, S. Zhou, and M. Xing, "Cooperative multitask learning for sparsity-driven SAR imagery and nonsystematic error autocalibration," in *IEEE Trans. Geoscience Remote Sensing*, vol. 58, no. 7, pp. 5132–5147, Jul. 2020, doi: 10.1109/TGRS.2020.2972972.

[17] M. Xing, X. Jiang, R. Wu, F. Zhou, and Z. Bao, "Motion compensation for UAV SAR based on raw radar data," *IEEE Trans. Geosci. Remote Sens.*, vol. 47, no. 8, pp. 2870–2883, Aug. 2009.

[18] L. Zhang, Z. Qiao, M.-D. Xing, L. Yang, and Z. Bao, "A robust motion compensation approach for UAV SAR imagery," *IEEE Trans. Geosci. Remote Sens.*, vol. 50, no. 8, pp. 3202–3218, Aug. 2012.
[19] W. Pu *et al.*, "Motion errors and compensation for bistatic forward-looking SAR with cubic-order processing," *IEEE Trans. Geosci. Remote Sens.*, vol. 54, no. 12, pp. 6940–6957, Dec. 2016.
[20] J. Torgrimsson, P. Dammert, H. Hellsten, and L. M. H. Ulander, "An efficient solution to the factorized geometrical autofocus problem," *IEEE Trans. Geosci. Remote Sens.*, vol. 54, no. 8, pp. 4732–4748, Aug. 2016.
[21] J. Wu, Y. Li, W. Pu, Z. Li, and J. Yang, "An effective autofocus method for fast factorized back-projection," *IEEE Trans. Geosci. Remote Sens.*, vol. 57, no. 8, pp. 6145–6154, Aug. 2019.
[22] W. Pu, J. Wu, Y. Huang, J. Yang, and H. Yang, "Fast factorized backprojection imaging algorithm integrated with motion trajectory estimation for bistatic forward-looking SAR," *IEEE J. Sel. Topics Appl. Earth Observ. Remote Sens.*, vol. 12, no. 10, pp. 3949–3965, Oct. 2019.
[23] L. Zhang, H.-L. Li, Z.-J. Qiao, M.-D. Xing, and Z. Bao, "Integrating autofocus techniques with fast factorized back-projection for high-resolution spotlight SAR imaging," *IEEE Geosci. Remote Sens. Lett.*, vol. 10, no. 6, pp. 1394–1398, Nov. 2013.
[24] N. Li, R. Wang, Y. Deng, W. Yu, Z. Zhang, and Y. Liu, "Autofocus correction of residual RCM for VHR SAR sensors with light-small aircraft," *IEEE Trans. Geosci. Remote Sens.*, vol. 55, no. 1, pp. 441–452, Jan. 2017.
[25] X. Fu, B. Wang, M. Xiang, S. Jiang, and X. Sun, "Residual RCM correction for LFM-CW mini-SAR system based on fast-time split-band signal interferometry," *IEEE Trans. Geosci. Remote Sens.*, vol. 57, no. 7, pp. 4375–4387, Jul. 2019.
[26] S. Zhou, L. Yang, L. Zhao, and G. Bi, "Quasi-polar-based FFBP algorithm for miniature UAV SAR imaging without navigational data," *IEEE Trans. Geosci. Remote Sens.*, vol. 55, no. 12, pp. 7053–7065, Dec. 2017.
[27] S. Zhou *et al.*, "A new fast factorized back projection algorithm for bistatic forward-looking SAR imaging based on orthogonal elliptical polar coordinate," *IEEE J. Sel. Topics Appl. Earth Observ. Remote Sens.*, vol. 12, no. 5, pp. 1508–1520, May 2019.
[28] M. D. Desai, and W. K. Jenkins, "Convolution backprojection image reconstruction for spotlight mode synthetic aperture radar," *IEEE Trans. Image Process.*, vol. 1, no. 4, pp. 505–517, Oct. 1992.
[29] W. Ye, T. S. Yeo, and Z. Bao, "Weighted least-squares estimation of phase errors for SAR/ISAR autofocus," *IEEE Trans. Geosci. Remote Sens.*, vol. 37, no. 5, pp. 2487–2494, Sep. 1999.
[30] T. J. Kragh and A. A. Kharbouch, "Monotonic iterative algorithm for minimum-entropy autofocus," in *Proc. Adapt. Sensor Array Process. (ASAP) Workshop*, vol. 53, pp. 1–38, Jun. 2006.
[31] L. Yang, M. Xing, Y. Wang, L. Zhang, and Z. Bao, "Compensation for the NSRCM and phase error after polar format resampling for airborne spotlight SAR raw data of high resolution," *IEEE Geosci. Remote Sens. Lett.*, vol. 10, no. 1, pp. 165–169, Jan. 2013.
[32] L. Yang, M. Xing, L. Zhang, J. Sheng, and Z. Bao, "Entropy-based motion error correction for high-resolution spotlight SAR imagery," *IET Radar, Son. Navig.*, vol. 6, no. 7, pp. 627–637, 2012.
[33] I. G. Cumming and F. H.-C. Wong, *Digital Processing of Synthetic Aperture Radar Data: Algorithms and Implementation*. Norwood, MA, USA: Artech House, 2005.

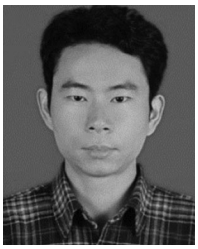

Min Bao (Member, IEEE) was born in Kunming, Yunnan, China, in 1984. He received the B.S. degree in electronics engineering, the M.E. degree in circuits and systems, and the Ph.D. degree in signal and information processing from Xidian University, Xi'an, China, in 2006, 2009, and 2012, respectively.

Since 2012, he has been working with Xidian University, and is currently working on the Teaching and Scientific Research Position of Grade 5 with School of Electronic Engineering, Xidian University. His research interests include SAR/ISAR applications.

Song Zhou (Member, IEEE) received the B.S. and M.S. degrees in telecommunication engineering and the Ph.D. degree in signal and information processing from Xidian University, Xi'an, China, in 2006, 2009, and 2013, respectively.

From January 2015 to February 2018, he was with the School of Electrical and Electronic Engineering, Nanyang Technological University, Singapore, as a full-time research fellow. He is currently with the School of Information Engineering, Nanchang University, Nanchang, China. His research interests include monostatic/bistatic SAR applications and motion error compensation.

Lei Yang (Member, IEEE) was born in Tianjin, China, in 1984. He received the B.S. degree in electronic engineering and the Ph.D. degree in signal and information processing from Xidian University, Xi'an, China, in 2007 and 2012, respectively.

From December 2012 to February 2017, he was with the School of Electrical and Electronic Engineering, Nanyang Technological University and Temasek Lab @ NTU as a full time Research Fellow and Research Scientist, respectively. He is currently with the Tianjin Key Lab For Advanced Signal Processing, Civil Aviation University of China, Tianjin, China, as an Associated Professor. His main research interests include high-resolution radar imaging and implementation, sparse Bayesian learning for radar imaging, etc.

Mengdao Xing (Fellow, IEEE) received the B.S. degree in electronic engineering and the Ph.D. degree in signal and information processing from Xidian University, China, in 1997 and 2002, respectively.

He is currently a Professor with the National Laboratory of Radar Signal Processing, Xidian University. He holds the appointment of Associate Dean of the Academy of Advanced Interdisciplinary Research. He has authored or coauthored more than 200 refereed scientific journal papers. He also has authored or co-authored two books about SAR signal processing. The total citation times of his research are greater than 8000. He was rated as Most Cited Chinese Researchers by Elsevier. He has more than 40 authorized China patents. His current research interests include synthetic aperture radar (SAR), inversed synthetic aperture radar (ISAR), sparse signal processing, and microwave remote sensing.

Dr. Xing's research has been supported by various funding programs, such as National Science Fund for Distinguished Young Scholars. He is currently the Associate Editor for radar remote sensing of the IEEE TRANSACTIONS ON GEOSCIENCE AND REMOTE SENSING.

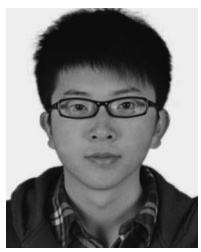

Lifan Zhao received the B.Sc. degree in electronic engineering from Xidian University, Xi'an, China, in 2010 and the Ph.D. degree from the School of Electrical and Electronic Engineering, Nanyang Technological University, Singapore, in 2016.

He is currently a Research Scientist with the Institute for Infocomm Research, A*STAR, Singapore. His research interests include statistical machine learning, Bayesian methods, compressed sensing, and their applications.